LA-UR- 01-5276
Approved for public release;
distribution is unlimited.

Title: **Polarization of Emission Lines from Beryllium-like Oxygen OV: Analysis Based on the Population-Alignment Collisional-Radiative Model**

Author(s): A. Iwamae, A. Tanaka, T. Inoue, T. Fujimoto, Honglin Zhang, D.P. Kilcrease and G. Csanak

Submitted to: Proceedings of the Third US-Japan Plasma Polarization Spectroscopy Workshop, Lawrence Livermore National Laboratory, June, 2001

Polarization of emission lines from beryllium-like oxygen OV: Analysis based on the Population-Alignment Collisional-Radiative model

Atsushi Iwamae, Akihiro Tanaka, Takeru Inoue and Takashi Fujimoto

Department of Engineering Physics and Mechanics, Graduate School of Engineering, Kyoto University

Kyoto 606-8501, Japan

Honglin Zhang, David P. Kilcrease and George Csanak,

Los Alamos National Laboratory, Los Alamos, NM, 87545, U.S.A.

Abstract

Longitudinal alignment of OV triplet lines for the ($2s3s\ ^3S_1 - 2s3p\ ^3P_{0,1,2}$) transitions is studied on the basis of a population-alignment collisional-radiative (PACR) model, which correlates quantitatively the observed polarization of emission lines from ions and atoms in a plasma with an anisotropy in the electron velocity distribution. The results are compared with measurements on the WT-3 tokamak at Kyoto University. The measured negative values of the longitudinal alignment are qualitatively explained from the anisotropic velocity distributions that have higher speed in the poloidal direction than that in the toroidal direction.

1. Introduction

It has been reported that emission lines may be polarized in magnetically confined plasmas [1,2,3]. This fact means that in addition to the intensity and the spectral profile of a line, we can use its polarization information in interpreting the conditions in the plasma. The triplet lines ($2s3s\ ^3S_1 - 2s3p\ ^3P_{0,1,2}$) of beryllium-like OV ions are often used in plasma diagnostics since the lines rather strong and the wavelengths are in the ultraviolet-visible region. It has been reported that the intensity ratio between the π component having the electric fields oscillating in the direction of the quantization axis, toroidal direction, and the σ component of the J=1 – 2 transition in the triplet lines changed during the discharge time [1]. This indicates that the ensemble of the upper levels ions is aligned. It is suggested that the spatially anisotropic collisional excitation by electrons having an anisotropic velocity distribution creates the alignment. In order to interpret the observed polarization of emission lines in terms of the anisotropic velocity distribution, we have constructed a kinetic model for the OV ions: the population-alignment collisional-radiative (PACR) model.

2. PACR model for OV ions

The levels of the $2s^2$, 2s2p, $2p^2$, 2s3s, 2s3p, and 2s3d configurations for OV (twenty levels) are considered in our model. Figure 1 shows the relevant part of the energy level diagram. The label numbers (1) to (20) are used to refer to the levels. The population densities are calculated for these twenty levels under the assumption that all transitions considered are optically thin and the plasma is the ionizing plasma.

In a PPS observation, the population and the alignment are determined for the upper level. The observed line intensity is given by the upper-level population and the radiative transition probability, and the degree of polarization of the observed line is given by the alignment, or the degree of the population imbalance, of the upper level. Thus a population $n(p)$ and alignment $a(p)$ are assigned to each level p. Transition probabilities and collision cross sections between the singlet levels are taken from the previous CR model for OV [4]. The alignment is considered only for the triplet levels. The excitation and deexcitation cross sections between a magnetic sublevel and a magnetic sublevel concerning anisotropic collisions are calculated by the distorted wave approximation for the transitions between levels (1)– (2), (3), (4) and (1) – (14), (15), (16) and (2), (3), (4) – (14), (15), (16) and for transitions between the different J levels in the same configuration i.e. (2) – (3), (4) and (3) – (4) and (14) – (15), (16) and (15) – (16).

For excitation and deexcitation of $a\,J \leftarrow a'J'$ ($a\,J \neq a'J'$) or $r \rightarrow p$ ($r \neq p$), the cross section data are the collision cross sections $Q_{a\,JM,a'J'M'}$ from a magnetic sublevel $a'J'M'$ to a magnetic sublevel $a\,JM$. As examples, the magnetic-sublevel-to-magnetic-sublevel cross sections $Q_{a\,JM,a'J'M'}$ from the ground state (1) $2s^2\ ^1S_0$ to (16) $2s3p\ ^3P_2$ and from (4) $2s3p\ ^3P_2$ to (16) $2s3p\ ^3P_2$ are tabulated in Table 1.

The collision cross sections employed in the PACR model are denoted by $Q_0^{kk'}(r,p)$. The cross section $Q_0^{00}(r,p)$ is the cross section from the population of level r to the population of level p; this is nothing but the conventional excitation cross section under isotropic collision conditions, $Q_0^{20}(r,p)$ is from population of level r to alignment of level p, $Q_0^{02}(r,p)$ from alignment of level r to population of level p,

and $Q_0^{22}(r,p)$ from alignment of level r to alignment of level p. These cross sections are related to the magnetic-sublevel-to-magnetic-sublevel cross sections as follows; [3]

$$Q_0^{00}(r,p)=(2J'+1)^{-1}\sum_{MM'}Q_{a\,JM,a'J'M'} \tag{2.1}$$

$$Q_0^{20}(r,p)=(2J'+1)^{-1}\sum_{MM'}(-1)^{J-M}<JJM-M\,|20>Q_{a\,JM,a'J'M'} \tag{2.2}$$

$$Q_0^{02}(r,p)=\sum_{M'}(-1)^{J'-M'}<J'J'M'-M'\,|20>\sum_{M}Q_{a\,JM,a'J'M'} \tag{2.3}$$

$$Q_0^{22}(r,p)=\sum_{MM'}(-1)^{J+J'+M+M'}<JJM-M\,|20><J'J'M'-M'|20>Q_{a\,JM,a'J'M'} \tag{2.4}$$

where $<JJM-M\,|kq>$ is the Clebsch-Gordan coefficient.

The converted excitation cross sections are plotted in Figure 2 (a) – (d) for the transition of (4) to (16) as an example. The plotted lines of the cross sections are the results of smooth spline interpolations for the calculated data. These cross sections concerning the alignment $a(p)$: $Q_0^{02}(r,p)$, $Q_0^{20}(r,p)$, $Q_0^{22}(r,p)$ may take negative values in contrast to the population to population cross sections $Q_0^{00}(r,p)$.

One example of the anisotropic electron velocity distributions is the existence of a beam component superimposed on bulk electrons having an isotropic distribution [5,6]. Another example is a Maxwellian distribution with different temperatures in different directions [7,8]. In order to quantify a velocity distribution,

it is expressed by $f(v,q)$, which satisfies the normalization condition, $\iint f(v,q)v^2\sin q\,\mathrm{d}v\mathrm{d}q=1$. Axial symmetry is assumed around the z-axis, the quantization axis. It is convenient to expand the velocity distribution in terms of Legendre polynomials,

$$f(v,q)=\sum_K f_K(v)P_K(\cos q) \tag{2.5}$$

where $P_K(\cos q)$ is the K th Legendre polynomial. The expansion coefficients are obtained by

$$f_K(v)=\frac{2K+1}{2}\int f(v,\cos q)P_K(\cos q)\sin q\,\mathrm{d}q\ . \tag{2.6}$$

Since it is impossible to distinguish between $\cos q$ and $\cos(p-q)$ components in an actual observation, only the K = (even) terms are considered.

We take the quantization axis in the magnetic field direction. In practice, the quantization axis is regarded as parallel to the toroidal direction. Two anisotropic velocity distribution models are assumed in the PACR model. In the first model, most of the electrons are described by the isotropic Maxwell velocity distribution and some of them have a shifted Maxwell distribution along the quantization z-axis centered at a high velocity V_z. These two parts are called the main $f_{\mathrm{M}}(v,q)$ and the child $f_{\mathrm{C}}(v,q)$ components;

$$f(v,q)=f_{\mathrm{M}}(v,q)+f_{\mathrm{C}}(v,q) \tag{2.7a}$$

$$f_{\mathrm{M}}(v,\theta)=\frac{2\pi}{1+d}\left(\frac{m}{2\pi k_{\mathrm{B}}T_{\mathrm{eM}}}\right)^{3/2}\exp\left(-\frac{m}{2k_{\mathrm{B}}T_{\mathrm{eM}}}v^2\right) \tag{2.7b}$$

$$f_{\mathrm{C}}(v,\theta)=\frac{2\pi d}{1+d}\left(\frac{m}{2\pi k_{\mathrm{B}}T_{\mathrm{eC}}}\right)^{3/2}\exp\left(-\frac{m}{2k_{\mathrm{B}}T_{\mathrm{eC}}}\left(v^2-2vV_z\cos\theta+V_z^2\right)\right), \tag{2.7c}$$

where d is the electron number ratio between the child and main components. This velocity distribution corresponds to the model of the runaway electrons in a main plasma in a tokamak.

In the second model, the electron velocity distribution is described by different electron temperatures; parallel and perpendicular to the quantization axis: the toroidal temperature T_{t} and the poloidal temperature T_{p}. The electron velocity distribution $f(v,\theta)$ is expressed as

$$f(v,\theta)=\left(\frac{m}{2\pi k_{\mathrm{B}}}\right)^{3/2}\left(\frac{1}{T_{\mathrm{p}}^2T_{\mathrm{t}}}\right)^{1/2}\exp\left\{-\frac{m}{2k_{\mathrm{B}}}\left[v^2\left(\frac{\sin^2\theta}{T_{\mathrm{p}}}+\frac{\cos^2\theta}{T_{\mathrm{t}}}\right)\right]\right\}. \tag{2.8}$$

It is noted that these two parameters called *temperature* here are not real temperatures, since the concept of electron temperature is based on the assumption that electrons obey the isotropic Maxwell velocity distribution. Temperature cannot be defined when we introduce the anisotropic velocity distribution. The shape of the equi-velocity surface of the distribution becomes "rugby-ball like" when the toroidal temperature is higher than the poloidal one, $T_{\mathrm{t}}>T_{\mathrm{p}}$, and "pancake-like" when $T_{\mathrm{t}}<T_{\mathrm{p}}$. Examples of the Legendre expansion coefficients $f_K(v)v^3$ (K=0,2,4) are shown in Figure 2 (e) – (f) for the distribution with two temperatures of T_{t} = 40 eV and T_{p} = 100 eV.

The excitation rate coefficients for the transitions $a\,J\leftarrow a'J'$, or $r\rightarrow p$, are defined with the following formula in the PACR model [3]:

$$C^{00}(r,p)=\int Q_0^{00}(r,p)2\,f_0(v)v^3\mathrm{d}v \tag{2.9a}$$

$$C^{20}(r,p)=\int Q_0^{20}(r,p)\frac{2}{5}f_2(v)v^3\mathrm{d}v \tag{2.9b}$$

$$C^{02}(r,p)=\int Q_0^{02}(r,p)\frac{2}{5}f_2(v)v^3\mathrm{d}v \tag{2.9c}$$

$$\begin{aligned}C^{22}(r,p)=&\int[Q_0^{22}(r,p)+Q_1^{22}(r,p)+Q_2^{22}(r,p)]\frac{2}{5}f_0(v)v^3\mathrm{d}v\\&+\int[2Q_0^{22}(r,p)+Q_1^{22}(r,p)-2Q_2^{22}(r,p)]\frac{2}{35}f_2(v)v^3\mathrm{d}v\\&+\int[6Q_0^{22}(r,p)-4Q_0^{22}(r,p)+Q_0^{22}(r,p)]\frac{2}{105}f_4(v)v^3\mathrm{d}v\end{aligned} \tag{2.9d}$$

where the $f_K(v)$ functions are the Legendre expansion coefficients defined above. The cross sections and the corresponding expansion coefficients in the integrands above are displayed in Figure 2.

Spontaneous radiative transition processes are isotropic, and we have only the two corresponding rates: for $r\rightarrow p$ ($p\neq r$).

$$A^{00}(r,p) = A(r,p) \tag{2.10a}$$

$$A^{22}(r,p) = (-1)^{J_r + J_p + 1}(2J_r + 1)\begin{Bmatrix} J_r & J_r & 2 \\ J_p & J_p & 1 \end{Bmatrix} A(r,p) \tag{2.10b}$$

where $A(r,p)$ is the usual Einstein A coefficient and $\{\}$ is the 6-j symbol.

We have two sets of rate equations for the ensemble of atoms. For population we have a rate equation

$$\begin{aligned} \frac{dn(p)}{dt} = & \sum_{r \neq p}\left[C^{00}(r,p)n_e + A^{00}(r,p)\right]n(r) \\ & -\left[\left\{\sum_{r \neq p} C^{00}(r,p) + S(p)\right\}n_e + \sum_{r \neq p} A^{00}(p,r)\right]n(p) \\ & + \sum_{r \neq p} C^{02}(r,p)n_e a(r) \\ & - C^{02}(p,p)n_e a(p) \end{aligned} \tag{2.11}$$

and for alignment we have

$$\begin{aligned} \frac{da(p)}{dt} = & \sum_{r \neq p} C^{20}(r,p)n_e n(r) \\ & - C^{20}(p,p)n_e n(p) \\ & + \sum_{r \neq p}\left[C^{02}(r,p)n_e + A^{22}(r,p)\right]a(r) \\ & - \left[C^{22}(p,p)n_e + \sum_{r \neq p} A^{00}(p,r)\right]a(p) \end{aligned} \tag{2.12}$$

where n_e is the electron density, $C^{20}(p,p)$ is the alignment production rate coefficient as given by the sum of the rate coefficient for the unequal depopulation from different magnetic sublevels and alignment production by elastic collisions, $C^{02}(p,p)$ is the rate of alignment decay by depopulation from the magnetic sublevels, and $C^{22}(p,p)$ is the rate coefficient for alignment destruction. The alignment destruction process has two components: inelastic and elastic collisions. The former is depopulation. The latter process may be called disalignment. At the moment, these rate coefficients are not available, so that we set $C^{02}(p,p) = 0$, $C^{20}(p,p) = 0$ and $C^{22}(p,p) = \sum_{r \neq p} C^{00}(p,r) + S(p)$. This corresponds to the assumption that the cross sections for the depopulation rate from the magnetic sublevels a_{JM} are all equal.

The population $n(p)$ and the alignment $a(p)$ for OV twenty levels are determined after solving the simultaneous equations under the steady state condition. The population $n(p)$ of the 2s3p $^3P_{0,1,2}$ levels; $n(14)$, $n(15)$ and $n(16)$ as a function of the electron density are shown in Figure 3 for the distribution with temperature components of T_t = 40 eV and T_p = 100 eV.

An ensemble of atoms is excited to the level p and the emission line for transition $p \to s$ is then observed from the direction perpendicular to the quantization axis. The intensity which is proportional to the population

$$I_0 = \frac{1}{4\pi l^2} n(p) A(p,s) \hbar w, \tag{2.13}$$

where l is the distance from the emitting atoms to the detector, is given by

$$I_{0\delta}=\frac{2}{3}(I_{\delta}+2I_{\acute{o}}). \tag{2.14}$$

The longitudinal alignment is defined as

$$A_{\mathrm{L}}=\frac{(I_{\delta}-I_{\acute{o}})}{(I_{\delta}+2I_{\acute{o}})}, \tag{2.15}$$

and the degree of polarization is related to the longitudinal alignment by

$$P=\frac{3A_{\mathrm{L}}}{A_{\mathrm{L}}+2}. \tag{2.16}$$

The intensities of the π and σ polarization components are given as [3]

$$I_{\delta}=\frac{1}{8\pi l^{2}}n(p)A(p,s)\hbar w[1+(-)^{J_P+J_s}\sqrt{6}(2J_p+1)\begin{Bmatrix}J_p & J_p & 2\\ 1 & 1 & J_s\end{Bmatrix}\frac{a(p)}{n(p)}] \tag{2.17a}$$

$$I_{\acute{o}}=\frac{1}{8\pi l^{2}}n(p)A(p,s)\hbar w[1-(-)^{J_P+J_s}\frac{\sqrt{6}}{2}(2J_p+1)\begin{Bmatrix}J_p & J_p & 2\\ 1 & 1 & J_s\end{Bmatrix}\frac{a(p)}{n(p)}]. \tag{2.17b}$$

From equations (2.15) and (2.17) the population $n(p)$ and alignment $a(p)$ are related to the longitudinal alignment,

$$A_L(p,s)=(-)^{J_P+J_s}\sqrt{\frac{3}{2}}(2J_p+1)\begin{Bmatrix}J_p & J_p & 2\\ 1 & 1 & J_s\end{Bmatrix}\frac{a(p)}{n(p)}. \tag{2.18}$$

For the observed lines OV 2s3s $^3\mathrm{S}_1-2\mathrm{s}3\mathrm{p}\ ^3\mathrm{P}_{1,2}$ the longitudinal alignments are calculated from

$$A_L(J=1\to1)=\sqrt{\frac{3}{8}}\frac{a(^3\mathrm{P}_1)}{n(^3\mathrm{P}_1)},\quad A_L(J=2\to1)=-\sqrt{\frac{7}{8}}\frac{a(^3\mathrm{P}_2)}{n(^3\mathrm{P}_2)}. \tag{2.19}$$

The longitudinal alignment of the 2s3p $^3\mathrm{P}_{0,1,2}$ levels; $A_{\mathrm{L}}(15,11)$ and $A_{\mathrm{L}}(16,11)$ as a function of the electron density are shown in Figure 3 for the two temperatures Maxwell distribution of equation (2.8) with T_{t} = 40 eV and T_{p} = 100 eV. The absolute values of A_{L} for both the transitions become large as n_{e} decreases and reach a plateau between 10^{18} and 10^{21} m^{-3}. The contour map of the longitudinal alignment $A_{\mathrm{L}}(16,11)$ is displayed in the three dimensional plot in Figure 4 for $n_{\mathrm{e}}=10^{18}$ m^{-3}. The range of T_{p} and T_{t} is between 10 and 300 eV.

The A_{L} value changes from 0.05 to –0.02 in the varied temperature range. Absolute values of A_{L} larger than 0.01 are realized only when the anisotropy of the velocity distribution is extremely large. From a close look into the calculation it is found that the alignment creation from the ground state plays the dominant role to produce polarization of the emission line. One third of $A_{\mathrm{L}}(16,11)$ is due to the alignment creation from the ground state, level (1), population to alignment of level (16). The next dominant contribution is alignment creation from the 2s2p $^3\mathrm{P}_{0,1,2}$ (2),(3),(4). Alignment to alignment transitions are less important.

For the double Maxwell distribution having a high velocity component given by equation (2.7), the calculated longitudinal alignment is less than 0.005 in absolute value for d values up to 0.2.

3. Experimental Observations

The WT-3 tokamak at Kyoto University is a middle-size toroidal plasma machine with a major radius of 0.65 m and a minor radius of 0.21 m. Typical discharge times are about 100 ms with $n_e = 3\times10^{18}$ m^{-3} and $T_e = 100$ – 300 eV. The plasma was produced in the joule-heating mode with a toroidal current of 60 kA to reach a stationary state at the one turn loop voltage of 2 V. The discharges are performed with hydrogen as a filling gas, and oxygen was the most common impurity.

The plasma was observed from slightly above the equatorial plane through a 15 mm-thick fused silica plate. Knife-edge blades light dump was equipped on the counter wall of the view port. Two plane mirrors and one concave mirror reduced the plasma image by a factor of one eighth which was focused on the entrance slit of a spectrometer. A one-meter focal length spectrometer (f/10) was equipped with a 3600 grooves/mm grating giving a reciprocal linear dispersion of 0.25 nm/mm at 280 nm. The spectrum was detected by an intensified CCD camera of 512×512 pixels (Princeton Instruments IMAX512T). Just behind the entrance slit we placed a calcite plate with thickness 5 mm. The crystal optic axis was in the horizontal direction at 30 ^{o} with respect to the surface normal. The normal incident light was separated into the ordinary (o) ray and the extraordinary (e) ray according to the polarization. Since the quantization axis in the toroidal direction, the π polarized component of the emission line is the e-ray (having the electric fields oscillating in the direction of the quantization axis) and the *s* light is the o-ray. The e-ray (π) was displaced parallel form the o-ray (σ) by about 0.5 mm. The polarization resolved spectral line intensity of the OV triplet lines (2s3s $^3S_1$ – 2s3p ^3P_J) 278.104 nm (J = 2), 278.803 nm (J = 1) and 278.986 nm (J = 0) was obtained. A typical spectral image is shown in Figure 5 which was recorded with an exposure time of 100 ms. The vertical *y*-axis corresponds to the distance over the plasma from the toroidal axis up to 80 mm. The sum of the counts over the *y*-axis is shown in Figure 6. Since several Fe II lines are observed with substantial intensity around the dominant OV triplet lines, the OV lines are fit with a nonlinear least square fitting routine over restricted fitting regions so as to eliminate the Fe II lines. Apparently the π components of the spectral lines were stronger than the σ components; this was due to the different reflectivities of the mirrors and grating for different polarized components. The relative sensitivity was calibrated by means of the unpolarized OV J=1-0 line (279.0 nm): The spontaneous emission of the transition from the J = 0 level to the J = 1 level is never polarized since there is only one upper magnetic sublevel (M_J = 0) and the relative intensity of π and σ light is equal in the observation perpendicular to the quantization axis. The relative sensitivity for the π/σ light components was determined to be 1.25 in the centeral region of the image and depens only slightly on the *y*-axis of the spectral image.

Ten pixels from the top in every one hundred pixels were binned in order to reduce the data transfer time. It made it possible to perform position and time resolved polarization spectroscopy. The six regions labeled (a) to (f) in Figure 5 correspond to plasma regions with 18.75 mm distant each in position from the plasma center. Each shot with 100 ms discharge period produced four frames of spectrum at six different positions in

plasma. The time evolution of the polarization resolved spectra of the region (b) is shown in Figure 7. This was taken with the exposure time of 3 ms with a 25.6 ms interval. Changes in relative intensity of the π and σ components are clearly seen, particularly for the $J = 1 - 2$ transition, indicating a change in the polarization degree of this line during the course of time. For instance, in the frame 3 (64.0 – 67.0 ms) of Figure 7, the apparent intensity of the σ light is comparable to the π light. Considering the relative sensitivity of our system, we conclude that the σ light intensity is stronger than the π light.

Each of the line intensities of the mutiplet spectra were evaluated after performing least square fits to the observed spectra. The relative sensitivity was corrected for, and the longitudinal alignment A_L was obtained according to equation (2.15). The longitudinal alignment A_L for the $J = 1 - 0$ line was confirmed to be 0 within the statistical uncertainty. This confirms that the relative sensitivity calibration was correct. Figure 8 shows the time evolution of the longitudinal alignments A_L for the $J = 1 - 2$ transition in six different positions in the plasma. A_L vary values between 0.050±28 and –0.078±16.

5. Comparison of calculation with measurement and discussion

The relatively large observed longitudinal alignment seen in an experiments was qualitatively explained in terms of the anisotropic electron distribution having the Maxwellian distribution with two temperature components rather than the double Maxwellian distribution with a high energy electron components. The higher toroidal temperature relative to the poloidal temperature causes the positive longitudinal alignment. The negative longitudinal alignment suggests that the poloidal component of the electron velocity distribution has a higher temperature than the toroidal one.

However the observed longitudinal alignment was at least four times larger than that simulated. This quantitative discrepancy may be explained by the following reasons: (i) The resonance structure of the cross section near the threshold energy may substantially contribute to alignment creation. (ii) The alignment creation by elastic scattering for the ion may play an important role. (iii) Alignment creation from the other triplet states, for example $2p^2\ ^3P_{0,1,2}$; (6), (7), (8), may be important.

Acknowledgment

This work is supported by the Grant-in-Aid for Scientific Research by Ministry of Education, Culture, Sports, Science and Technology. Work at Los Alamos National Laboratory has been performed under the auspices of the U.S. Department of Energy.

Reference

[1] T. Fujimoto, H. Sahara, T. Kawachi, T. Kallstenius, M. Goto, H. Kawase, T Furukubo, T. Maekawa and Y. Terumichi, Phys. Rev. E **54** R2240 (1996).

[2] T. Fujimoto and S. A. Kazantsev, Plasma Phys. Control. Fusion **39** 1267 (1997).

[3] T. Inoue, M. Nakai, A. Tanaka, K. Kawakami, A. Iwamae, T. Fujimoto, M. Yoshikawa and T. Tamano, Plasma Phys. Control. Fusion **43** L9 (2001).

[4] T. Kato, J. Lang and K.A. Berrington, NIFS-DATA-2 (1990).

[5] L. Pieroni and S. E. Segre, Phys. Rev Lett. **34** 928 (1975).

[6] B. Coppi, F. Pegoraro, R. Pozzoli and G. Rewoldt, Nucl. Fusion **16** 309 (1976).

[7] J. C. Kieffer, J. P. Matte, H. Pépin. M. Chaker, Y. Beaudoin, T. W. Johnston, C. Y. Chien, S. Coe, G. Mourou and J. Dubau, Phys. Rev. Lett. **68** 480 (1992).

[8] M. D. Bowden, T. Okamato, F. Kimura, H. Muta, K. Uchino, K. Muraoka, T. Sakoda, M. Maeda, Y. Manabe, M. Kitagawa and T. Kimura, J. Appl. Phys. **73** 2732 (1993).

[9] T. Fujimoto and F. Koike, K. Sakimoto, R. Okasaka, K. Kawasaki, K. Takiyama, T. Oda and T. Kato, NIFS-DATA-16 (1992).

Table 1. The cross section between a magnetic sublevel to a magnetic sublevel for the transitions from (a) (1) – (16) the ground state $2s^2\ ^1S_0$ (M_J' = 0) to $2s3p\ ^3P_2$ (M_J = 0, ±1, ±2) and (b) (4) – (16) $2s2p\ ^3P_2$ (M_J' = 0, ±1, ±2) to $2s3p\ ^3P_2$ (M_J = 0, ±1, ±2). Axial symmetry is assumed.

(a)

Electron energy E / eV	Cross section from M_J' = 0 to M_J = 0	to M_J = ±1	to M_J = ±2
		$Q(E)$ / cm^2	
12.0403	1.04521E-19	8.17786E-20	1.35507E-20
12.0715	1.03336E-19	8.08635E-20	1.34462E-20
12.1951	9.90237E-20	7.74690E-20	1.28051E-20
12.3984	9.24614E-20	7.22801E-20	1.17364E-20
12.6775	8.47100E-20	6.60254E-20	9.97166E-21
13.4432	6.49552E-20	5.08011E-20	8.33905E-21
14.4471	4.72833E-20	3.69040E-20	5.76629E-21
15.6435	3.23014E-20	2.53166E-20	4.36215E-21
19.2021	1.11021E-20	8.88879E-21	2.24898E-21
23.3392	3.60141E-21	2.99308E-21	1.16808E-21
27.7258	1.24059E-21	1.08102E-21	6.02280E-22
32.3221	4.63036E-22	4.24347E-22	3.08281E-22
41.7698	8.59680E-23	8.64815E-23	8.80221E-23
51.4268	2.18730E-23	2.36907E-23	2.91437E-23
61.1941	7.02377E-24	8.04687E-24	1.11162E-23

(b)

Electron energy E / eV	Cross section from $M_J' = 0$ to $M_J = 0$	to $M_J = \pm 1$	to $M_J = \pm 2$
		$Q(E)$ / cm^2	
11.1485	2.34744E-18	1.70406E-19	4.52239E-20
11.1821	2.33830E-18	1.68291E-19	4.46328E-20
11.3155	2.30395E-18	1.60609E-19	4.27339E-20
11.5343	2.23967E-18	1.48155E-19	4.00266E-20
11.8338	2.15643E-18	1.32003E-19	3.60549E-20
12.6507	1.94774E-18	1.00423E-19	2.86709E-20
13.7128	1.71506E-18	7.11771E-20	2.20616E-20
14.9680	1.48109E-18	4.91073E-20	1.72482E-20
18.6558	9.84364E-19	1.98474E-20	1.17041E-20
22.8919	6.48249E-19	9.14213E-21	9.75923E-21
27.3503	4.42624E-19	4.85780E-21	8.54905E-21
32.0006	3.13724E-19	2.82647E-21	7.41573E-21
41.5216	1.76636E-19	1.14160E-21	5.43006E-21
51.2254	1.11539E-19	5.17039E-22	3.83851E-21
61.0249	7.64851E-20	2.54041E-22	2.68155E-21

(b) continued

Electron energy E / eV	Cross section from $M_J' = \pm 1$ to $M_J = \mp 2$	to $M_J = \mp 1$	to $M_J = 0$	to $M_J = \pm 1$	to $M_J = \pm 2$
			$Q(E)$ / cm^2		
11.1485	4.42067E-20	5.02090E-20	1.83033E-19	2.38336E-18	8.56024E-20
11.1821	4.35935E-20	4.96339E-20	1.80678E-19	2.37253E-18	8.49790E-20
11.3155	4.14134E-20	4.74677E-20	1.72540E-19	2.33132E-18	8.25821E-20
11.5343	3.84410E-20	4.42557E-20	1.58711E-19	2.26060E-18	7.93536E-20
11.8338	3.47546E-20	4.04043E-20	1.40189E-19	2.16821E-18	7.53451E-20
12.6507	2.56123E-20	3.23935E-20	1.05692E-19	1.94552E-18	6.54321E-20
13.7128	1.78667E-20	2.58278E-20	7.36013E-20	1.70114E-18	5.61203E-20
14.9680	1.17713E-20	2.13637E-20	4.96543E-20	1.46314E-18	4.82568E-20
18.6558	3.82307E-21	1.63479E-20	1.87129E-20	9.77051E-19	3.47444E-20
22.8919	1.20622E-21	1.43055E-20	8.15900E-21	6.54495E-19	2.49855E-20
27.3503	4.36052E-22	1.26892E-20	4.27116E-21	4.55852E-19	1.76000E-20
32.0006	1.77791E-22	1.10585E-20	2.51004E-21	3.29384E-19	1.21229E-20
41.5216	4.12122E-23	8.12613E-21	1.05132E-21	1.91294E-19	5.76967E-21
51.2254	1.29206E-23	5.75125E-21	4.88330E-22	1.23528E-19	2.79306E-21
61.0249	4.89951E-24	4.01978E-21	2.43474E-22	8.60392E-20	1.41691E-21

(b) continued

Electron energy E / eV	Cross section from $M_J' = \pm 2$ to $M_J = \mp 2$	to $M_J = \mp 1$	to $M_J = 0$	to $M_J = \pm 1$	to $M_J = \pm 2$
			$Q(E)$ / cm^2		
11.1485	5.84639E-39	4.42067E-20	9.98760E-20	1.65487E-19	2.31378E-18
11.1821	5.90279E-39	4.35935E-20	9.87813E-20	1.63880E-19	2.30161E-18
11.3155	6.09932E-39	4.14134E-20	9.36142E-20	1.57303E-19	2.25192E-18
11.5343	6.35860E-39	3.84410E-20	8.63724E-20	1.46792E-19	2.18515E-18
11.8338	6.76808E-39	3.47546E-20	7.90231E-20	1.34667E-19	2.09816E-18
12.6507	7.56812E-39	2.56123E-20	5.96823E-20	1.06966E-19	1.88068E-18
13.7128	8.81844E-39	1.78667E-20	4.33781E-20	8.22747E-20	1.64370E-18
14.9680	1.05388E-38	1.17713E-20	3.14257E-20	6.35210E-20	1.41796E-18
18.6558	1.55036E-38	3.82307E-21	1.65816E-20	3.73499E-20	9.77370E-19
22.8919	1.84060E-38	1.20622E-21	1.14654E-20	2.47243E-20	6.89876E-19
27.3503	1.83840E-38	4.36052E-22	9.17029E-21	1.70476E-20	5.07921E-19
32.0006	1.64056E-38	1.77791E-22	7.65435E-21	1.17287E-20	3.86336E-19
41.5216	1.20535E-38	4.12122E-23	5.47278E-21	5.63198E-21	2.42758E-19
51.2254	4.72630E-38	1.29206E-23	3.84814E-21	2.74538E-21	1.65318E-19
61.0249	1.83779E-37	4.89951E-24	2.68418E-21	1.39847E-21	1.19392E-19

Figure Captions

Figure 1 Energy level diagram of the levels included in the present PACR model calculation. The spectroscopic transitions observed are from levels (14), (15), (16) to (11).

Figure 2 An example of the cross sections for 2s2p $^3P_2$ level (14) and 2s3p $^3P_2$ level (16). (a) population to population $Q_0^{00}(r,p)$, (b) population to alignment $Q_0^{20}(r,p)$ (c) alignment to population $Q_0^{02}(r,p)$ and (d) alignment to alignment $Q_0^{22}(r,p)$ The Legendre expansion coefficients of the velocity distribution having two temperatures T_p, = 100 eV and T_t = 40 eV that are used to obtain the rate coefficients are plotted under the corresponding cross sections. See equation (2.9) (e) $f_0(v)v^3$. (f) $f_2(v)v^3$. (g) The dash-dotted line is $f_4(v)v^3$ with $f_0(v)v^3$ and $f_2(v)v^3$.

Figure 3 The electron density n_e dependence of (a) the population of level (14) (dash-dotted line), level (15) (broken line) and level (16) (thick line). (b) the longitudinal alignment $A_L(15,11)$ (broken line) and $A_L(16,11)$ (thick line) for the two temperatures T_p = 100 eV and T_t = 40 eV

Figure 4 The dependence of the longitudinal alignment $A_L(16,11)$ on the toroidal and poloidal temperatures. The electron density n_e is 10^{18} m^{-3}.

Figure 5 A full image of the polarization resolved OV triplet lines ($2s3s\ ^3S_1 - 2s3p\ ^3P_{0,1,2}$), 278.104 nm ($J$ = 1 – 2), 278.803 nm (J = 1 – 1) and 278.986 nm (J = 1 – 0) obtained from WT-3. The right of each pair is the π-light having the electric fields oscillating in the direction of the toroidal axis, left s -light. The exposure time is 100 ms. The ordinate corresponds to the distance from the plasma center. The labelled (a)-(f) regions are binned over 10-pixels each for the position- and time-resolved polarization measurements.

Figure 6 A polarization resolved spectrum of the OV triplet with the fitting.

Figure 7 Time evolution of the OV triplet spectra of the region b (Shot No 83831). Note that in frame 3 (64.0-67.0 ms) for the 1-2 transition the intensity of the π light is weaker than that of σ light i.e. longitudinal alignment is substantially negative.

Figure 8 Longitudinal alignment of the J = 1 – 2 emission line observed from different positions in the plasma.(a) line of sight crosses at 86 mm (b) 67 mm, (c) 48 mm, (d) 30 mm (e) 11 mm and (f) –8 mm from the center.

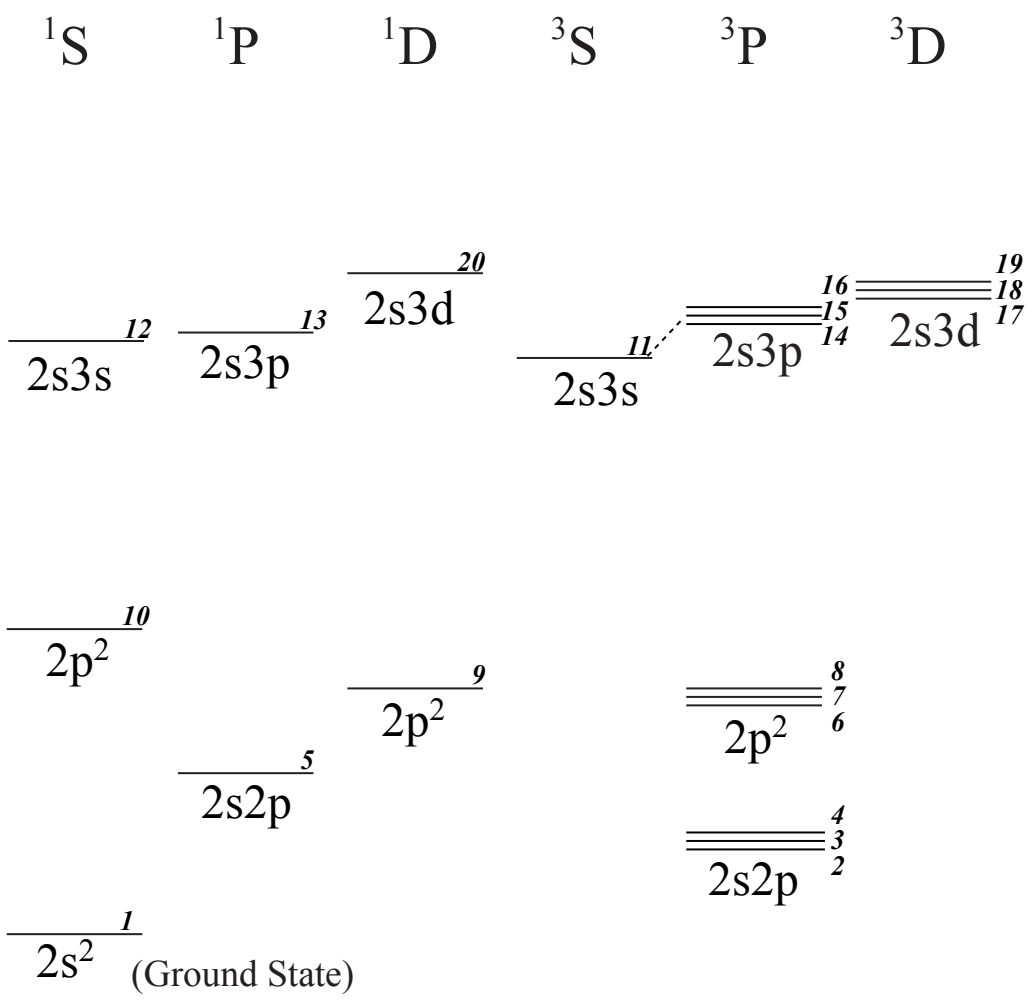
1S
1P
1D
3S
3P
3D
20
2s3d
12
2s3s
13
2s3p
11
2s3s
16
15
14
2s3p
19
18
17
2s3d
10
2p2
9
2p2
8
7
6
2p2
5
2s2p
4
3
2
2s2p
1
2s2
(Ground State)

Figure 1

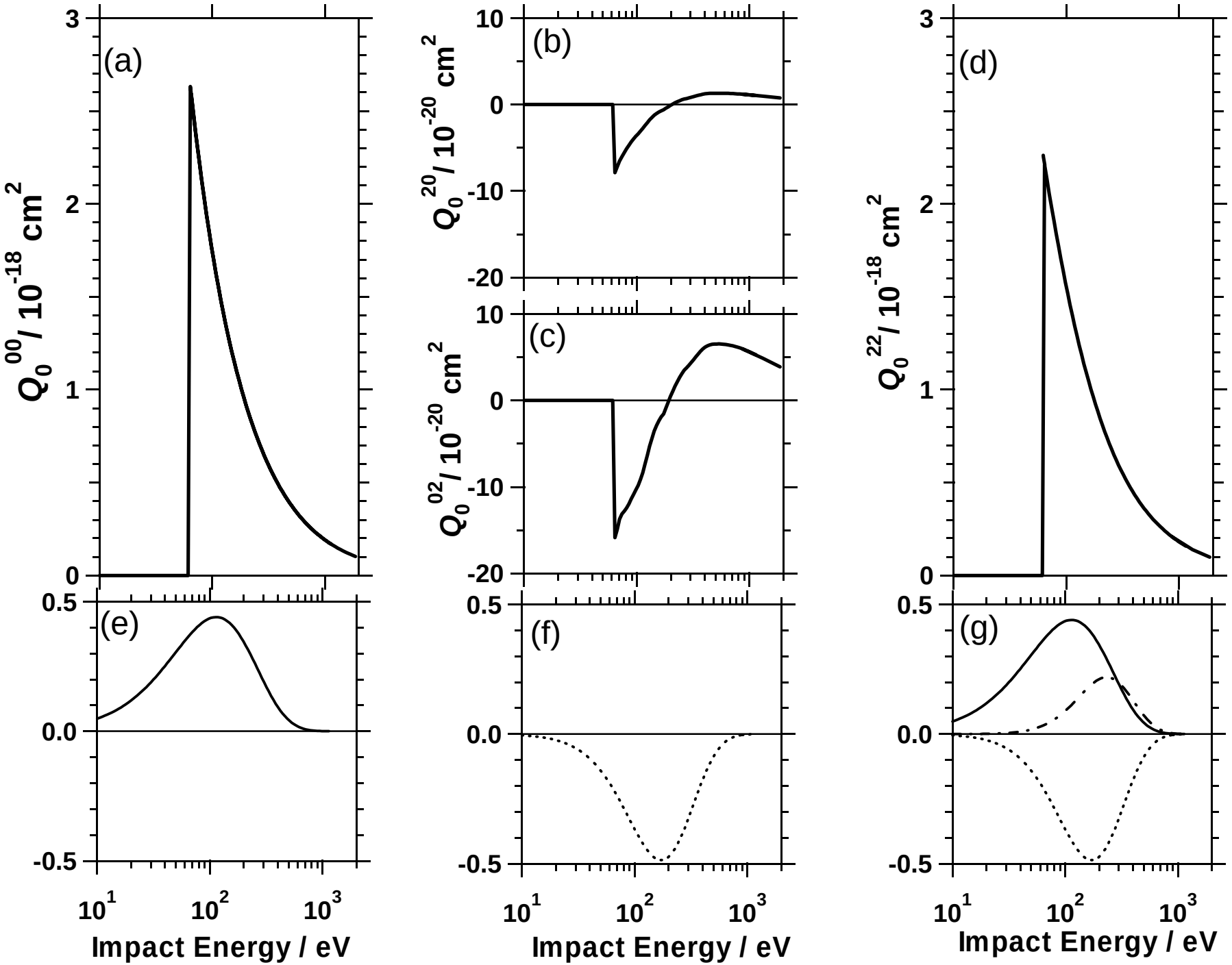
(a)
(b)
(c)
(d)
(e)
(f)
(g)
Q_0^{00} / 10^{-18} cm^2
Q_0^{20} / 10^{-20} cm^2
Q_0^{02} / 10^{-20} cm^2
Q_0^{22} / 10^{-18} cm^2
Impact Energy / eV
Impact Energy / eV
Impact Energy / eV

Figure 2

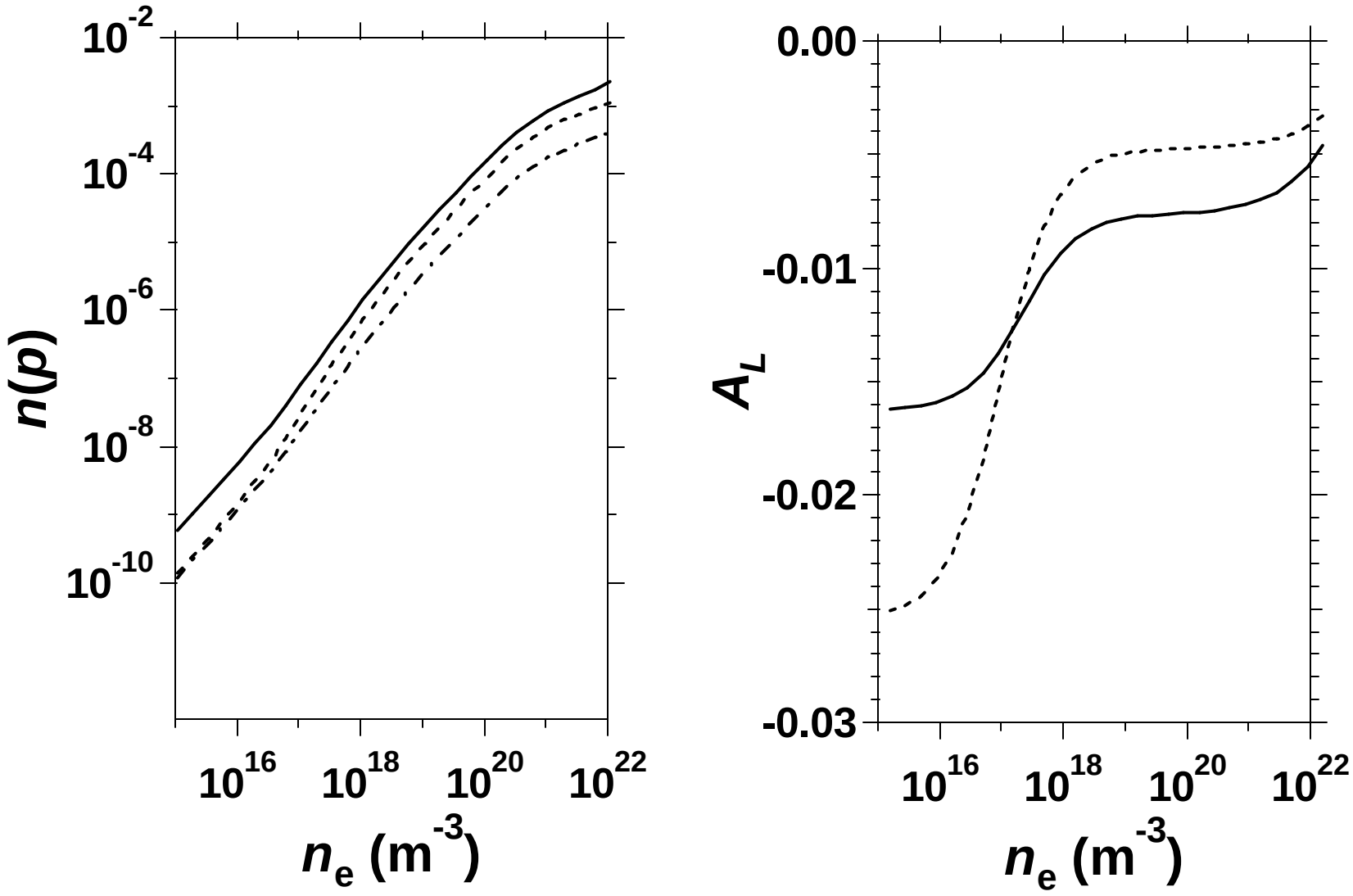
10^-2
10^-4
10^-6
10^-8
10^-10
n(p)
10^16
10^18
10^20
10^22
n_e (m^-3)
0.00
-0.01
-0.02
-0.03
A_L
10^16
10^18
10^20
10^22
n_e (m^-3)

Figure 3

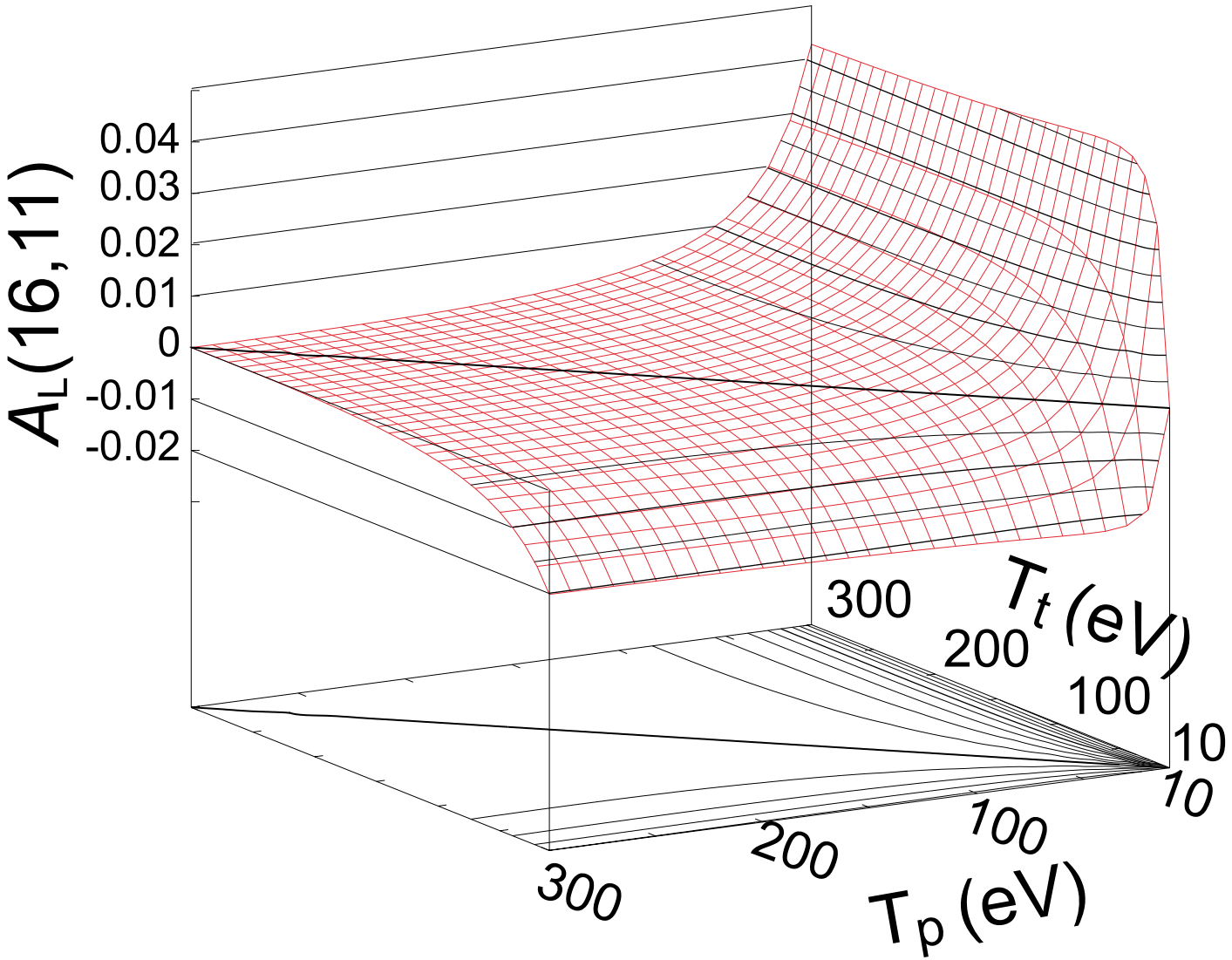
$A_L(16,11)$
0.04
0.03
0.02
0.01
0
-0.01
-0.02
300
200
100
10
T_t (eV)
300
200
100
10
T_p (eV)

Figure 4

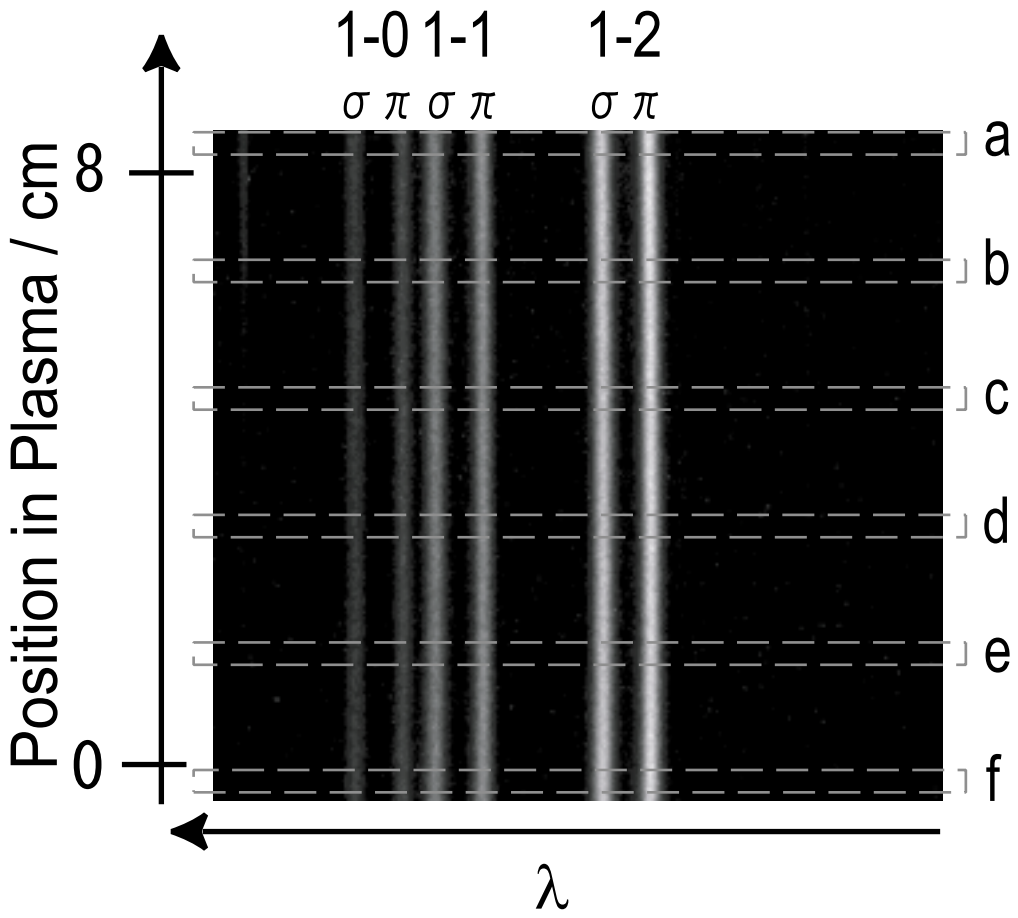

Figure 5

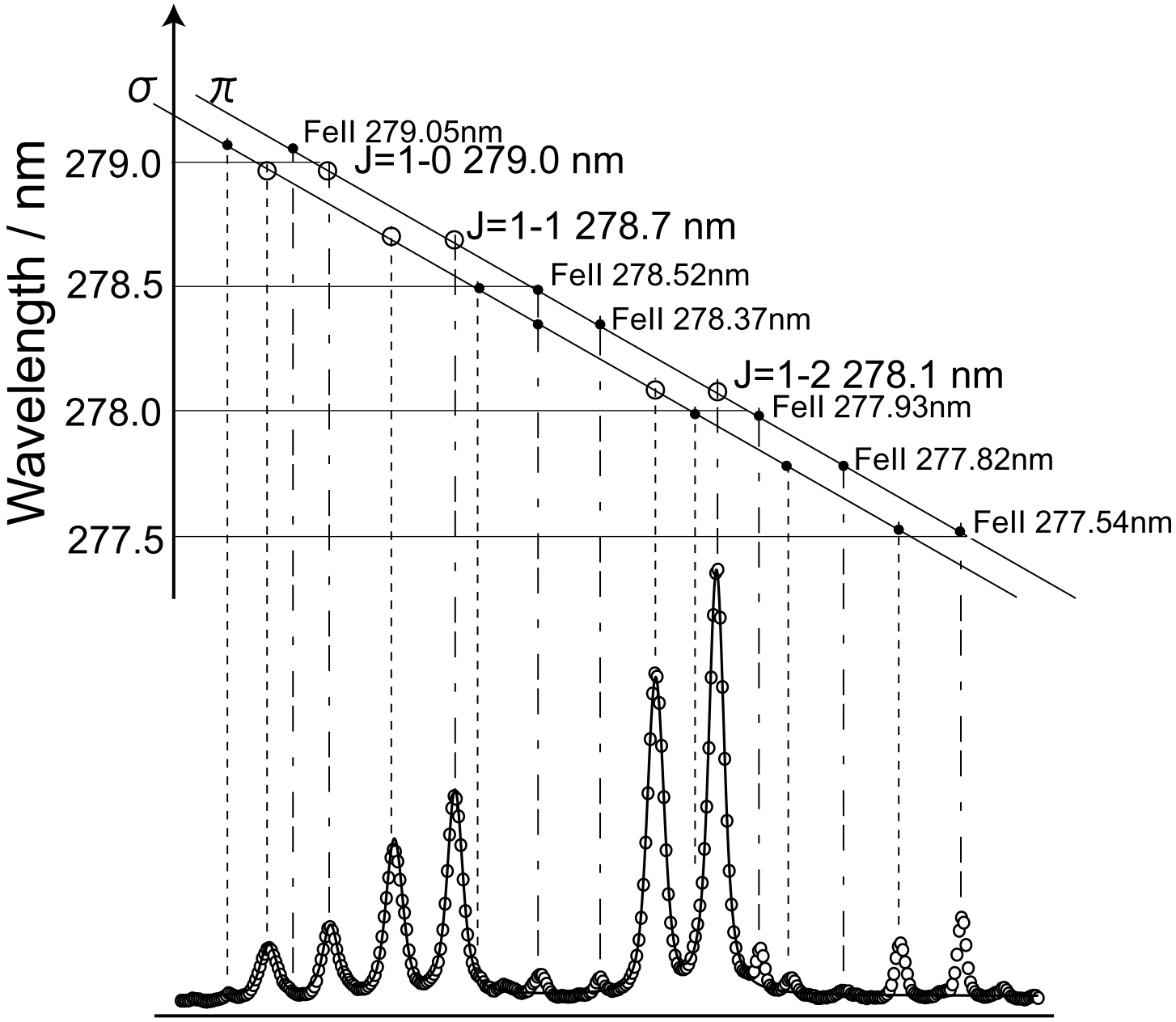
σ
π
Wavelength / nm
279.0
278.5
278.0
277.5
FeII 279.05nm
J=1-0 279.0 nm
J=1-1 278.7 nm
FeII 278.52nm
FeII 278.37nm
J=1-2 278.1 nm
FeII 277.93nm
FeII 277.82nm
FeII 277.54nm

Figure 6

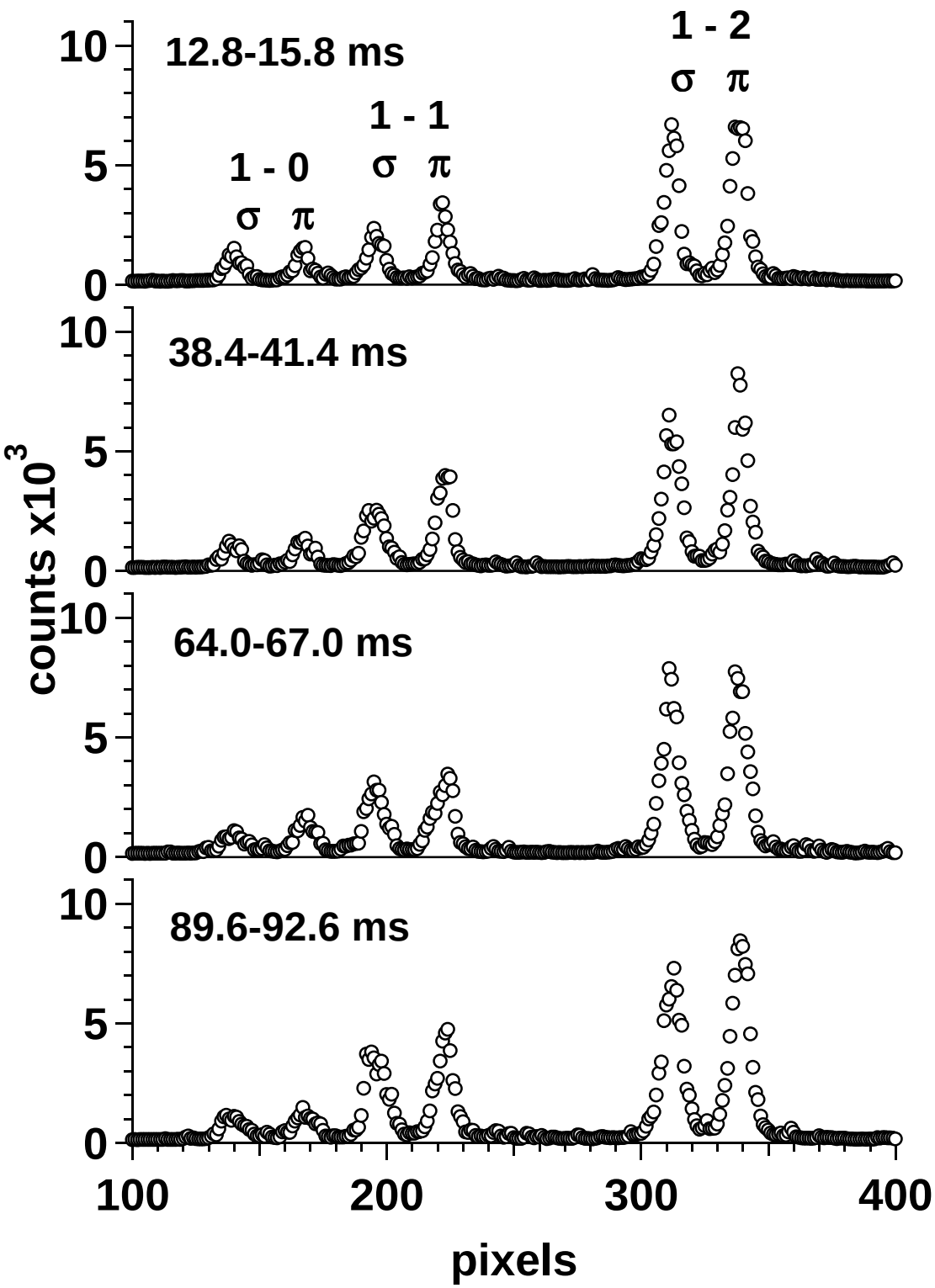
12.8-15.8 ms
1 - 0
σ π
1 - 1
σ π
1 - 2
σ π
38.4-41.4 ms
64.0-67.0 ms
89.6-92.6 ms
counts x10^3
pixels
0
5
10
100
200
300
400

Figure 7

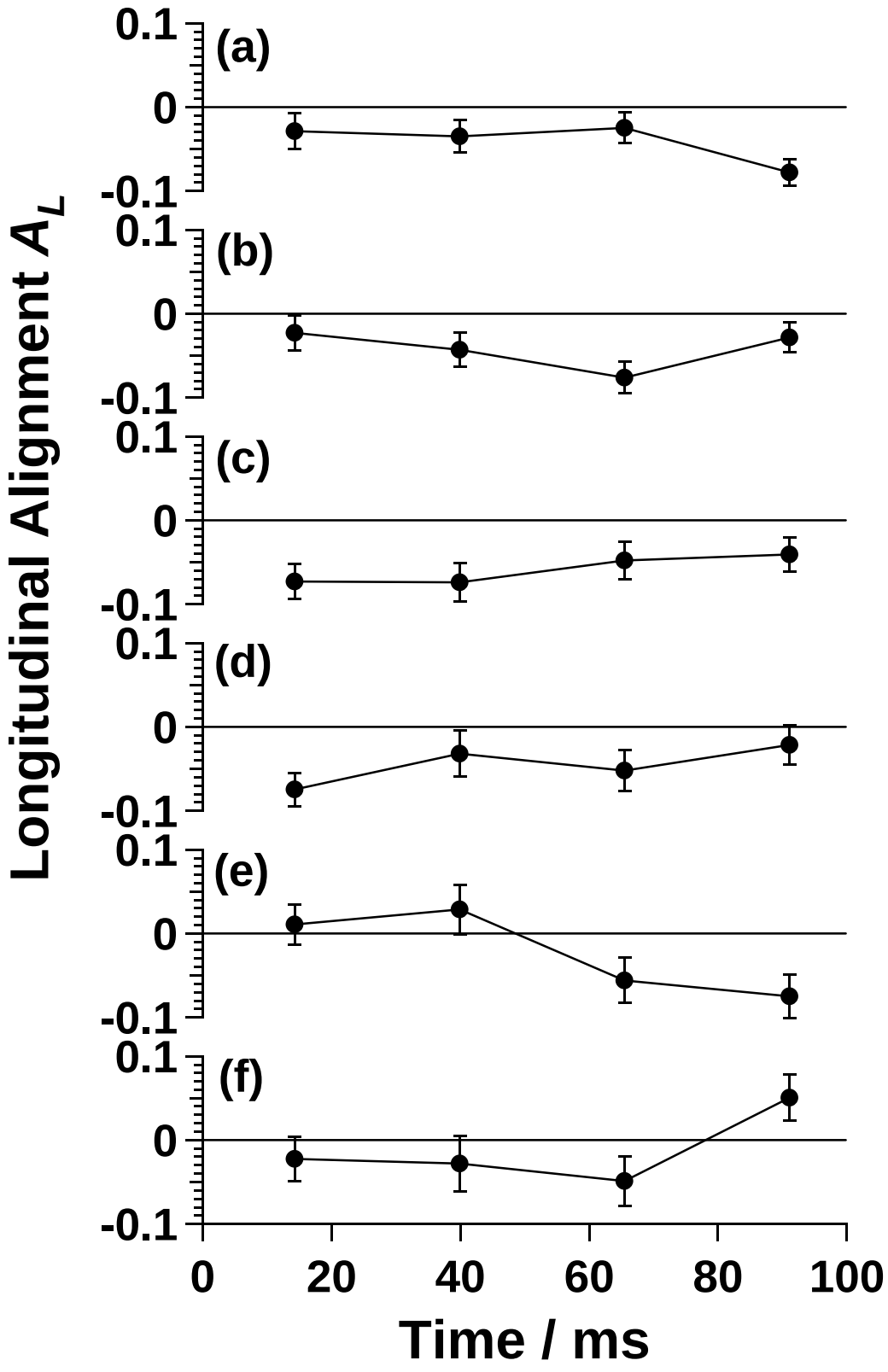
Longitudinal Alignment A_L
(a)
(b)
(c)
(d)
(e)
(f)
0.1
0
-0.1
0
20
40
60
80
100
Time / ms

Figure 8